

OPEN ACCESS

Simulating the Impact of Glassy Carbon Foam Electrodes on the Performance of Sodium Iodine Batteries

To cite this article: F. Gerbig *et al* 2023 *J. Electrochem. Soc.* **170** 040517

View the [article online](#) for updates and enhancements.

You may also like

- [The Use of Zinc-Bromine Battery Technology to Remove and Recover Zinc from Scrap and Waste Steel Resources](#)
Rhys David Standing, Christian James Laycock, Richard M Dinsdale *et al.*
- [Influence of Metal Oxide Coatings on the Microstructural and Electrochemical Properties of Different Carbon Materials](#)
Jesse J. Wouters, M. Isabel Tejedor-Tejedor, Julio J. Lado *et al.*
- [Influence of Metal Oxide Coatings, Carbon Materials and Potentials on Ion Removal in Capacitive Deionization](#)
Jesse J. Wouters, M. Isabel Tejedor-Tejedor, Julio J. Lado *et al.*

Investigate your battery materials under defined force!
The new PAT-Cell-Force, especially suitable for solid-state electrolytes!



- Battery test cell for force adjustment and measurement, 0 to 1500 Newton (0-5.9 MPa at 18mm electrode diameter)
- Additional monitoring of gas pressure and temperature

www.el-cell.com +49 (0) 40 79012 737 sales@el-cell.com

EL-CELL[®]
electrochemical test equipment





Simulating the Impact of Glassy Carbon Foam Electrodes on the Performance of Sodium Iodine Batteries

F. Gerbig,^{1,z} M. Holzapfel,² and H. Nirschl¹

¹Institute of Mechanical Process Engineering and Mechanics, Karlsruhe Institute of Technology (KIT), Straße am Forum 8, 76131 Karlsruhe, Germany

²Fraunhofer Institute for Chemical Technology (ICT), Joseph-von-Fraunhofer-Straße 7, 76327 Pfinztal, Germany

This publication examines the influences of glassy carbon foam electrodes on the overall battery performance of secondary sodium iodine batteries. The battery combines a molten sodium anode and an iodine-based cathode with NaSICON serving as a ceramic separator. The battery system works at 100 °C and is suitable for stationary energy storage. A long cycle life and good resource utilization are major concerns for establishing the proposed battery system. This paper employs a spatially resolved simulation approach to investigate the effects of foam electrodes of different porosities and cell sizes on the charging and discharging behavior. The spatially resolved model reflects species and mass transport as well as electrochemical processes and reactions in the positive half cell. An open-pored glassy carbon foam cathode structure shows an improved utilizable capacity compared to a simpler two-dimensional electrode. Parameter studies of foam porosity and specific surface area indicate that porosity is the crucial parameter for achievable depth of discharge. We conclude that glassy carbon open-pored foam of preferably high porosity is a suitable material for cathode electrodes in sodium iodine batteries.

© 2023 The Author(s). Published on behalf of The Electrochemical Society by IOP Publishing Limited. This is an open access article distributed under the terms of the Creative Commons Attribution 4.0 License (CC BY, <http://creativecommons.org/licenses/by/4.0/>), which permits unrestricted reuse of the work in any medium, provided the original work is properly cited. [DOI: 10.1149/1945-7111/accab7]



Manuscript submitted November 28, 2022; revised manuscript received March 29, 2023. Published April 18, 2023.

Lithium-ion batteries are among the most widespread battery types and state-of-the-art battery technologies for mobile devices and automotive applications due to their superior energy and power density. However, the expected demand of electric vehicles will outstrip lithium supply in the near future leading to increasing lithium prices.¹ Additionally, the decarbonization of the energy sector is a major challenge for limiting the effects of climate change. The large-scale integration of clean energy sources destabilizes the energy grid because of intermittent penetration by renewable energy sources.² Electrochemical energy storage can alleviate the urgent need for grid energy storage but asks for earth-abundant, cost-efficient, and lithium-free solutions. The all-liquid sodium iodine battery combines a molten sodium anode with an aqueous iodine cathode. The battery operates at about 100 °C, which is above the melting point of the sodium anolyte and the boiling point of the aqueous catholyte. It is a future candidate for medium-scale stationary energy storage application due to its high specific capacity and sustainable materials.^{3,4} Numerical investigations have indicated transport limitation as the major restriction for the overall battery performance.⁵ To overcome these limitations, an improved cathode electrode structure needs to provide a large surface area for the surface reactions inside the battery maintaining a high porosity to achieve sufficient energy capacities and resource efficiency of the battery system. Three-dimensional electrodes are commonly used to surmount transport limitations in two-dimensional electrodes in electrochemical processes.⁶ Packed-bed electrodes, porous electrodes, active fluidized-bed electrodes, and moving-bed electrodes are realizations of three-dimensional electrodes.⁷ Among these, porous structures like cloths, felts, or foams are best suited for the targeted sodium iodine battery because of their simplicity and cost advantage which are desired in stationary energy storage. Open-pored foams are one potential cathode geometry⁸ and have been considered for lead flow batteries.⁹ Metal foams are widely described in the literature and serve—for instance—as catalysts or are used for heat transfer applications.^{10,11} Solid foams are utilized for high-strength materials in the aviation industry. In most cases, foams are manufactured by mixing the liquid material with a blowing agent. The foam solidifies after cooling. Therefore, minimal surface structures mathematically describe dry foams. The Kelvin

cell is the most prominent one and is widely used for idealized descriptions of foams.¹² It is a 14-sided tetrakaidecahedron consisting of six quadrilateral and eight hexagonal faces. Weaire and Phelan proposed a structure with even smaller surface area.¹³ However, the difference in surface area is less than 0.3%, and the Weaire-Phelan structure is more complex consisting of six 14-sided polyhedra and two 12-sided polyhedra with irregular faces. It is computationally expensive to build and simulate virtual Weaire-Phelan foams and implement appropriate cyclic boundary conditions. Studies of the mechanical properties and heat transfer in foams indicate negligible differences between the Kelvin cell and Weaire-Phelan cell models.^{14,15} Therefore, the present work focuses on Kelvin's conjecture. The Kelvin cell is space-filling, and the foam unit cell results from subtracting a sphere from the Kelvin cell.¹⁶ The cell size determines the parent bubble size of the foam. The porosity and pore sizes depend on the ratio between Kelvin cell size and sphere diameter. This method produces foams of arbitrary length and thickness by packing the resulting foam unit cells.

A variety of materials are feasible for constructing such open-pored foam structures including polymers, carbon materials, or different metals. Most traditional battery electrode materials are not chemically stable in the aggressive iodine media but glassy carbon shows long-term stability against the catholyte solution.³ As a consequence, reticulated vitreous carbon (RVC) foams—also known as glassy carbon foams—are suitable candidates for sodium iodine batteries. Reticulated vitreous carbons are commonly fabricated from a resin-coated, open-cell polyurethane foam through carbonization at 700 °C–1100 °C. The foam evolution process includes drainage by capillary forces and rapid wall thinning which results in Kelvin cell-like open-pored foam structures. Tenorino and Casolo-Ginelli first describe a reticulated, three-dimensional electrode obtained by metallization of polyurethane foams in an electrochemical process.¹⁷ A 2009 review emphasizes reticulated vitreous carbon as a new carbon material for batteries.¹⁸ Electrochemically active species penetrate the high void volumes of up to 97%, thus achieving high volumetric energy densities. The rigid structure withstands temperatures of around 100 °C. In addition, reticulated vitreous carbons are inexpensive, available, possibly produced from sustainable materials, and inert against various chemicals including halides. Mastragostino and Gramellini reported kinetic studies with vitreous carbon electrodes and the bromine/bromide redox couple in an aqueous solution.¹⁹

^zE-mail: felix.gerbig@kit.edu

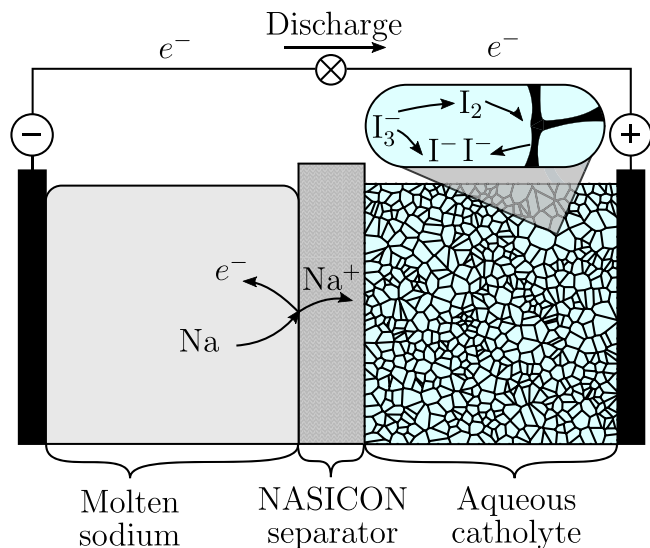


Figure 1. Working principle of a sodium iodine battery with glassy carbon foam cathode structure.

Table I. Modeling parameters for the Na-I₂ secondary battery.

Parameter	Value
Symmetry factors (α_a, α_c)	0.5
Cathode conductivity (σ_{cath})	$2 \times 10^4 \text{ S m}$
Cathode length (l_{cath})	2 cm
Separator thickness (l_{sep})	0.5 mm
Exchange current factor i_0°	1 A cm^{-2}
NaSICON conductivity (σ_{sep}) ³³	10 mS cm^{-1}
Diffusion coefficients Na ⁺ (D_{Na^+}) ³⁴	$6.3867 \times 10^{-9} \text{ m}^2 \text{ s}^{-1}$
Diffusion coefficients I ⁻ (D_{I^-}) ³⁵	$7.8625 \times 10^{-9} \text{ m}^2 \text{ s}^{-1}$
Diffusion coefficients I ₃ ⁻ ($D_{\text{I}_3^-}$) ³⁵	$5.2677 \times 10^{-9} \text{ m}^2 \text{ s}^{-1}$
Diffusion coefficients I ₂ (D_{I_2}) ³⁵	$5.9989 \times 10^{-9} \text{ m}^2 \text{ s}^{-1}$

The objective of this paper is to introduce three-dimensional electrodes and to establish an improved cathode architecture for sodium iodine batteries. To fill this gap in the literature, the present paper identifies an optimized cell design by performing spatially resolved electrochemical simulations of glassy carbon foam electrodes. Our findings aid in developing competitive aqueous iodine cathodes with high reversible efficiency and power density.

Mathematical Model

This section outlines the physical model of a liquid sodium iodine battery and details the enhanced cathode structures used in this publication. Zhu and Kee describe the underlying electrochemical model in great detail.⁴ Previous work extends their one-dimensional model to three dimensions with the necessary additions.⁵ The present study fully resolves the positive electrode with a three-dimensional simulation because there, the chemistry and thermodynamic constraints are the most complex and the geometry has a decisive influence on the overall battery performance. The negative half cell solely contains of molten sodium which does not influence the cell voltage and battery performance much because of its high conductivity. Its effect is modeled by a boundary condition.

The presented simulations were carried out with the OpenFOAM® software package, which is based on the finite volume method.²⁰ The software was originally designed for computational fluid dynamics. The code is partially rewritten by means of the implementation of governing equations and boundary conditions for

the underlying electrochemical model. The numerical solver is an adaption from a previously developed lithium-ion battery solver^{21,22} to describe the sodium iodine battery.⁵ Figure 1 illustrates the sodium iodine battery working principle. The chemical reaction directions are shown for the discharging process.

Electrochemical model.—The net reaction of the sodium iodine battery is



with a standard potential of 3.2495 V.^{23,24} The anode contains molten sodium slightly above its melting point at 100 °C. NaSICON (Na Super Ionic CONductor) separates the cathode and anode half cells and is a pure sodium-ion conductor. It is a dense ceramic material and serves as electrolyte separator membrane. NaSICON-type ceramics commonly feature a high sodium ion conductivity at relatively low temperatures and negligible interfacial resistance to liquid sodium.^{25,26} Furthermore, it displays good stability against molten sodium²⁷ and concentrated aqueous halide solutions³ which makes it an attractive alternative electrolyte to established sodium- β'' alumina. While discharging, the molten sodium level in the anode compartment sinks, and sodium ions travel through the NaSICON separator entering the cathode domain. The cathode half cell is made up of a glassy carbon foam infiltrated with electrolyte. The aqueous electrolyte comprises I₂, I⁻, I₃⁻, and Na⁺. Iodide forms from iodine at the electrolyte-cathode electrode interface. At the same time, iodine is reproduced from the equilibrium reaction between iodine, iodide, and triiodide:²⁸



This is important because iodine itself is barely soluble in water but can recombine with iodide to polyiodides which prevents precipitation of potentially harmful solid iodine. Triiodide formation occurs in a two-step mechanism but globally follows the reaction state in Eq. 2. The surface fluxes \mathbf{J}_k and molar production rates r_k contribute to the species transport in the electrolyte solution:

$$\frac{\partial [X_k]}{\partial t} = -\nabla \cdot \mathbf{J}_k + r_k \quad [3]$$

The diffusion and migration components are estimated by dilute solution theory and govern the electrolyte species surface fluxes^{29,30}

$$\mathbf{J}_k = -D_k^{\text{el}} \nabla [X_k] - \frac{z_k F}{RT} D_k^{\text{el}} [X_k] \nabla \Phi_{\text{el}} \quad [4]$$

where $[X_k]$ are the molar concentrations of the electrolyte species, D_k^{el} are the corresponding diffusion coefficients, z_k are the corresponding charges, F is the faradaic constant, R is the universal gas constant, T is the temperature, and Φ_{el} is the electrostatic potential in the catholyte solution. The electrolyte charge fluxes result from the movement of the charge-carrying species:

$$\mathbf{i}_{\text{el}} = -\sigma_{\text{el}} \nabla \Phi_{\text{el}} - \sum z_k F D_k^{\text{el}} [X_k] \quad [5]$$

The electric current density field is divergence-free $\nabla \cdot \mathbf{i}_{\text{el}} = 0$ because of the imposed local charge neutrality in the electrolyte. The present study does not resolve double layer forming and thus yields $\frac{\partial \Phi_{\text{el}}}{\partial t} = 0$. In the glassy carbon foam structure, Ohm's law represents the current density:

$$\nabla \cdot \mathbf{i}_{\text{ed}} = 0 \quad [6]$$

The crucial charge transfer kinetics between glassy carbon surface and the electrolyte follow the widely accepted Butler-Volmer equation.^{29,31}

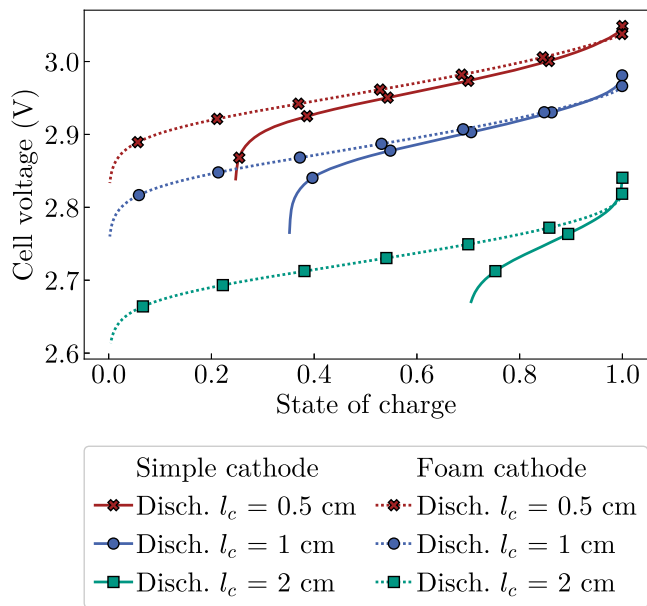


Figure 2. Comparison of cell voltage curves between simple cathode design and foam structure built of Kelvin unit cells with 1 mm length. The curves represent the C/5 discharge. Electrolyte initial concentrations correspond to 8.3 M in the fully discharged state.

$$i_{BV} = i_0 \left[\exp\left(\frac{\alpha_a F}{RT}(\Phi_{cd} - \Phi_{el} - U_{eq}([X_k]))\right) - \exp\left(-\frac{\alpha_c F}{RT}(\Phi_{cd} - \Phi_{el} - U_{eq}([X_k]))\right) \right] \quad [7]$$

It is a phenomenological modeling approach to express the net charge transfer rate resulting from the heterogeneous reaction occurring on the electrolyte-cathode surface. The Butler-Volmer current density depends on the local overpotential along with the exchange current density i_0 which accounts for the reaction kinetics and takes the form Ref. 4:

$$i_0 = i_0^\circ \frac{([I_2][I_2]^{*-1})^{\beta_a/2} ([I^-][I^-]^{*-1})^{1-\beta_a}}{1 + ([I_2][I_2]^{*-1})^{1/2}} \quad [8]$$

where i_0° fits the exchange current density to experimental data.³² Table I lists the modeling parameters used in this study.

Foam characterization.—Reticulated vitreous carbon foams incorporate a high volumetric porosity and are chemically inert and therefore serve as the cathode structures. It is important to quantitatively describe the foam properties in order to understand their effects on the battery performance. The foam structures can be characterized by means of porosity ϵ and the specific surface area. The mathematical construction of a Kelvin foam structure is achieved by subtracting a sphere from Kelvin's conjecture. The porosity is defined as the ratio between the empty volume fraction and the total volume. It can take values between 0 and 1:

$$\epsilon = \frac{V_{\text{empty}}}{V} \quad [9]$$

It is sufficient to look at one Kelvin unit cell because it is packable and symmetric in each direction.³⁶ The volume of the Kelvin unit cell then equals the total volume ($V = V_{\text{Kel}}$). The Kelvin cell volume is obtained by subtracting six square pyramids with height h off the octahedron volume:³⁷

$$V_{\text{Kel}} = V_{\text{Octahedron}} - 6V_{\text{square pyramid}} = 8\sqrt{2} \left(\frac{l_{\text{pyramid}}}{3} \right)^3 \quad [10]$$

The void space calculates from the spherical parent bubble $V_{\text{bub,Kel}}$ by subtracting 14 sphere caps V_{cap} which protrude the truncated octahedron sides:

$$V_{\text{empty}} = V_{\text{bub,Kel}} - 8V_{\text{cap,hexagon}} - 6V_{\text{cap,square}} \quad [11]$$

The spherical cap volumes depend on the parent bubble diameter l_{bub} :

$$V_{\text{cap}} = \frac{\pi h^2}{3} \left(\frac{3}{2} l_{\text{bub}} \right) \quad [12]$$

The specific surface area SSA describes the total surface area per bulk volume which, in the case of a Kelvin foam structure, takes the form:

$$SSA_{\text{foam,Kel}} = \frac{S_{\text{foam,Kel}}}{V_{\text{Kel}}} \quad [13]$$

The total surface area is obtained by subtracting the curved areas of the 14 spherical caps from the parent bubble surface

$$S_{\text{foam,Kel}} = S_{\text{bub,Kel}} - 8S_{\text{cap,hexagon}} - 6S_{\text{cap,square}} \quad [14]$$

with $\{S_{\text{cap,hexagon}}, S_{\text{cap,square}}\} \in \mathbb{R}_{\geq 0}$. The curved area of a spherical cap is calculated by Ref. 38:

$$S_{\text{cap}} = \pi l_{\text{bub}} h \quad [15]$$

State of charge and operating window.—The state of charge (SoC) defines the level of charge in a battery relative to its maximal capacity and takes values between 0 (empty) and 1 (full). The SoC is useful comparing the state of batteries with different sizes or specific capacities. The achievable SoC is a helpful measure to determine the resource efficiency of a battery configuration. The depth of discharge (DoD) is an alternative form for the same measure for the discharging process.

$$\text{SoC} = 1 - \text{DoD} = \left(\frac{\int [\text{Na}^+]_{(x,t)} dV_{\text{el}}}{V_{\text{el}}} - [\text{Na}^+]_0 \right) \times \frac{1}{[\text{Na}^+]_{\text{max}} - [\text{Na}^+]_0} \quad [16]$$

The utilizable volumetric capacity sets the capacity of the battery utilized in a charge or discharge cycle in relation to the cell volume. It is a measure for the battery performance.

$$c_{v,u} = F \frac{\int ([\text{Na}^+]_{\text{start}} - [\text{Na}^+]_{\text{end}}) dV_{\text{el}}}{V_{\text{cell}}} \quad [17]$$

The operating window of the sodium iodine battery is determined by three limits of use in the cathode half cell. Firstly, the local sodium ion concentration must not exceed $[\text{NaI}]_{\text{max}}$ to avoid precipitation of sodium iodide. Secondly, the local elemental iodine concentration ($[I]_{\text{tot}} = [I^-] + 2[I_2] + 3[I_3^-]$) must yield $[I_{\text{tot}}]/[\text{Na}^+] < 0.475$ for iodine to stay in solution.³⁹ Thirdly, iodide and triiodide may not completely deplete at the electrode surface during the discharge process because they serve as the charge-carrying species for the Butler-Volmer reaction. Otherwise, the charge transfer reaction discontinues and discharging terminates.

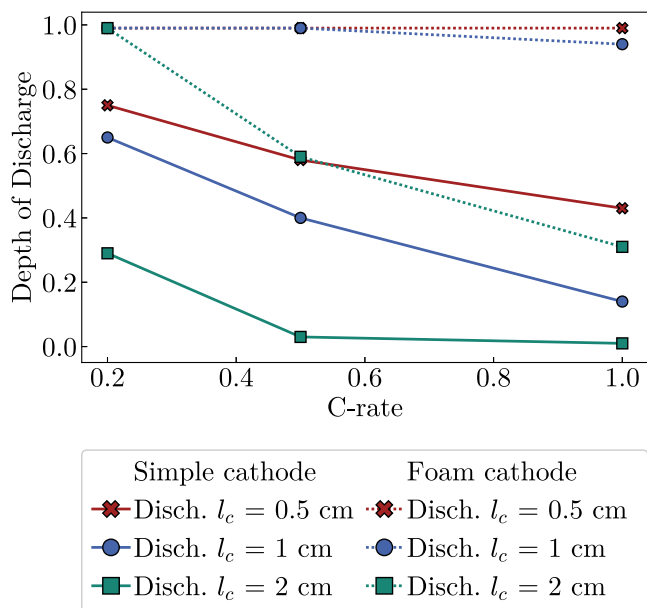


Figure 3. Comparison of cell performance between the simple cathode design and the foamy cathode structure built of Kelvin unit cells with 1 mm length. The reached depth of discharge is shown for different cathode lengths (l_c) and C-rates. Electrolyte initial concentrations correspond to 8.3 M in the fully discharged state.

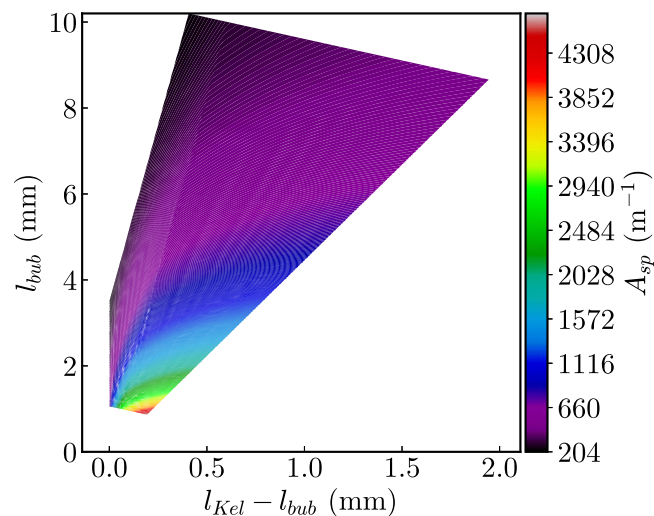


Figure 4. Specific surface area of open-pored foam structures based on Kelvin's conjecture.

Results and Discussion

The following section outlines the model-predicted influences of three-dimensional glassy carbon foam cathode electrodes on the battery performance. Glassy carbon is a widely used material for battery electrode structures, inert and of high electric conductivity, and therefore serves as the current-collecting foam material for the following investigations.⁴⁰ The simulations were conducted on a hex-dominant computational grid with approximately two million cells and 2.5×10^{-4} m cell size in the bulk electrolyte. Local grid refinement reduces the cell size to $30 \mu\text{m}$ in high-gradient areas. The time step ranges between $\Delta t = 1$ s and $\Delta t = 10$ s depending on the C-rate. It is considerably lower at the beginning and the end of cycling to capture the larger potential changes.

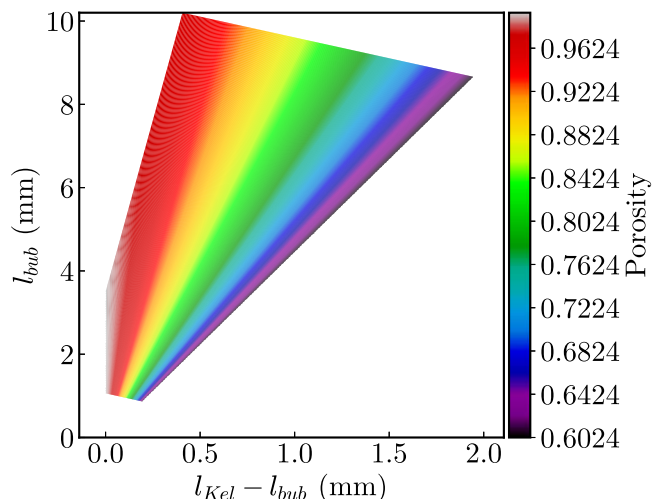


Figure 5. Porosity of open-pored foam structures based on Kelvin's conjecture.

Comparison between simple and three-dimensional foam cathode design.—Former studies used a two-dimensional cathode design to investigate various influences on the overall battery performance of the sodium iodine battery.⁵ A vertically placed, round-shaped titanium disc served as cathode structure. Despite its simplicity, the main shortcoming of this design is that the electrode surface is constrained to a small area in the cathode compartment. In light of the unsatisfactory active species utilization of such a design, the scope of the presented work includes exploring structures that overcome this limitation.

A preliminary study uses a Kelvin cell design.⁴¹ Here, the cathode electrode foam structure infiltrated with electrolyte provides a larger and more evenly distributed surface. Figure 2 shows the discharge curves for both cell designs considering different cathode lengths l_c at a 1/5 C-rate. Discharging starts at the fully charged state and stops immediately when the species concentration of NaI or I_2 exceeds the solubility limit. The species concentrations in the fully charged state are evaluated by the iodine solubility relations.^{5,39} With increasing cathode length, discharging terminates earlier for the two-dimensional cell design. Whereas discharging simulations based on the cathode compartment filled with the glassy carbon foam structure based on Kelvin's conjecture nearly reach fully discharged states at SoC = 0. Hereby, the cathode length does not influence reachable SoC, thus influencing cell voltage. The external current density is proportional to the electrolyte volume when the C-rate is held constant. Therefore, the batteries with thicker cathode half cells cause higher ohmic resistances and overpotentials leading to lower cell voltages. Figure 3 shows the achievable DoD for the discharge process considering different C-rates and cathode lengths. Again, the two-dimensional cathode design and the foamy cathode design are compared. Discharging results in insufficient achievable DoDs for the majority of simulation cases with a two-dimensional cathode design. Solely low C-rates of 0.2 C and 0.5 cm cathode length lead to a DoD higher than 0.5. Using the foamy cathode design drastically improves the DoD to nearly 1 for cathode lengths of 0.5 cm and 1 cm. The simulated battery with a 2 cm cathode compartment length reaches a high utilizable capacity for 0.2 C but decreases for higher C-rates.

Variation of foam structure.—After demonstrating enhanced battery performance using three-dimensional electrodes in preliminary simulations, the following section examines their effects in greater detail. Accordingly, we vary the virtual foam structure and monitor its impact on the overall battery performance. The main objective is to predict the best possible cathode electrode structure of sodium iodine batteries.

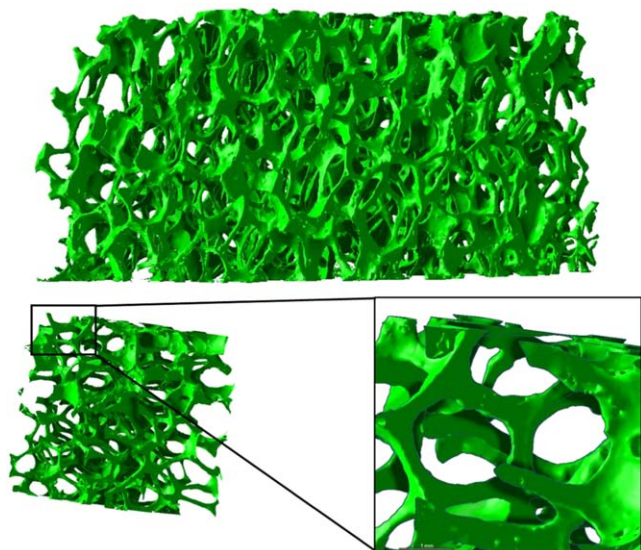


Figure 6. μ CT scan of a glassy carbon foam.

Properties of regular open-pored foams.—First, it is necessary to understand how the directly controllable variables affect the specific surface area (A_{sp}) and porosity, respectively.

Figures 4 and 5 illustrate the specific surface area and the porosity dependent on the parent bubble size l_{bub} along with the difference between the length of the Kelvin cell and parent bubble size ($l_{Kel} - l_{bub}$). The latter can be interpreted as the shell thickness of the foam bubbles.

The values calculate from the equations describing the geometry of Kelvin's conjecture in the foam characterization section.

The shell thickness is constrained to a certain range to remain mechanically stable (lower bound) and still produce open pores (upper bound). It is generally assumed that a high surface area and high porosity are both beneficial for the battery performance. High porosity means that the cathode electrode structure takes less space leaving the bigger volume part for the electrolyte which then increases the energy density. A high specific surface area promises lower overpotentials and lower specific molar production rates at the electrode surface. The latter may avoid an early termination of battery cycling due to the local depletion or precipitation of molar species. Porosity and specific surface area are two of the key parameters used in the literature to account for the battery microstructure and morphology in homogenized battery models.^{42,43} Figure 5 depicts that increasing the parent bubble size while holding the shell thickness constant (which corresponds to going up on the y-axis) increases the porosity. Simultaneously, the specific surface area decreases (Fig. 4). Contrarily, the specific surface area grows with increasing shell thickness (advancing on the x-axis) while the

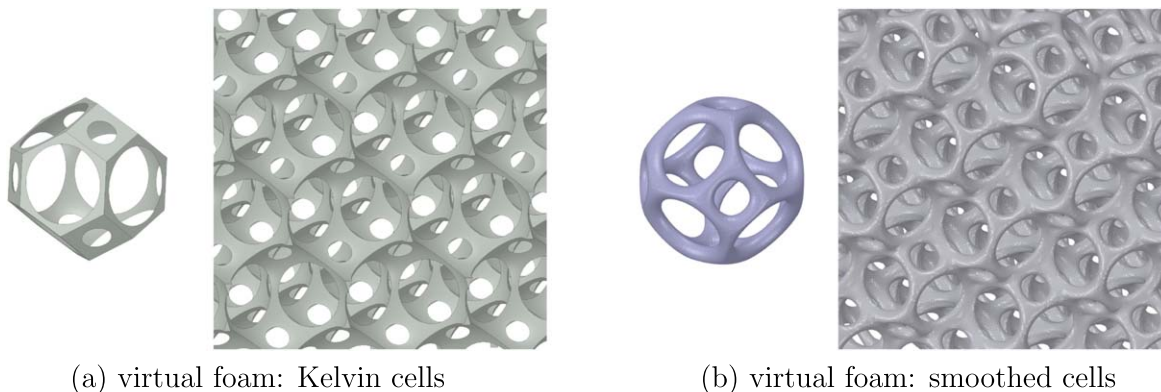
porosity diminishes. As a consequence, one property cannot maximize without minimizing the other.

Foam creation.—First, a comparison of the virtual foams with experimentally made glassy carbon foams assures the transferability of the simulation results to real batteries: Fig. 6 shows the reconstruction of a μ CT scan of a glassy carbon open-pored foam. In the manufacturing process, a commercial polyurethane-based filter foam (10 ppi) was impregnated repeated times with phenol-formaldehyde resin (molar ratio 1:2.5) and dried. The dried filter foam was then heated under argon with 5 K/min to 300 °C, followed by 10 K/min to 600 °C and 20 K/min to 1350 °C, which was kept for 5 h followed by natural cooling to room temperature. The foam mainly consists of larger parent bubbles, which are subdivided by around nine pores of similar sizes. The pore size is approximately 2.5 mm and the parent bubble size is about 4 mm.

The basic structure is regular and correlates well to the foam unit cell derived from Kelvin's conjecture. However, the μ CT scans reveal thicker struts of the real foams compared to the Kelvin cell-based virtual foam structures. In addition, the foam edges are less sharp—especially at the pores—in comparison to the virtual Kelvin foam cells. The foam junctures of the experimentally manufactured foam are thickened which is an effect of the material solidification process. Therefore, additional effort is necessary to create a more realistic unit cell. The Blender software offers algorithms for manipulating and smoothing of virtual shapes which were applied to the Kelvin cell foam structures.⁴⁴ Figure 7 compares a foam based on the Kelvin unit cells and a foam based on the smoothed unit cells. The smoothed cells approximation better captures the key features of the glassy carbon foams. The quality of the virtual foam structure toward a more realistic glassy carbon foam representation can be enhanced using smoothing algorithms. The following studies are based on the smoothed virtual cell design for this reason.

With the aid of the aforementioned method, twelve different smoothed virtual foam structures are created modifying the strut thickness and the cell size. The overall length of the cathode is fixed at 2 cm. Table II lists the porosity and the specific surface area of the examined virtual foam structures. The data elucidates two trends: First, porosity solely correlates with strut diameter and lowers with increasing value. The thinnest strut in this study leads to the highest porosity of 97.4% while the porosity of the thickest foam is about 40% lower. They represent the highest and lowest porosities achievable with this method yielding sensible strut thicknesses and pore sizes. Second, the specific surface area follows the opposite trend and increases with the strut size but also with increasing number of cells. The specific surface area of the foam structure with 1 mm cell size and the highest strut diameter is about 26 times larger than the shown structure with the lowest surface area.

Discharging.—Figure 8 outlines the termination states for a galvanostatic C/4 discharging process for the twelve foam structures



(a) virtual foam: Kelvin cells

(b) virtual foam: smoothed cells

Figure 7. Comparison between foam structures based on the Kelvin cell (a) and foam structures with additional manipulation and smoothing (b).

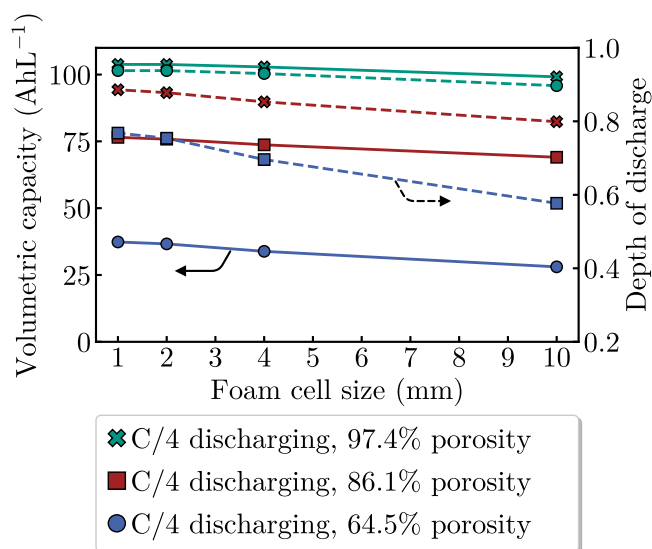


Figure 8. The solid lines represent the utilizable volumetric capacity of a sodium iodine battery with glassy carbon foam structures as current collectors while dashed lines represent the corresponding depth of discharge as a function of the foam cell size. Under C/4 discharging, the green lines represent a porosity of 97.4%, the red lines represent a porosity of 86.1%, and the blue lines represent a porosity of 64.6%.

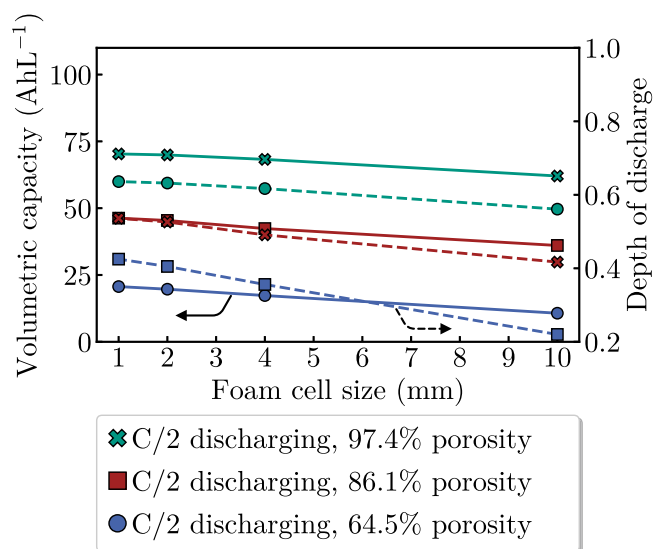


Figure 9. The Solid lines represent the utilizable volumetric capacity of a sodium iodine battery with glassy carbon foam structures as current collectors while the dashed lines represent the corresponding depth of discharge as a function of the foam cell size. Under C/2 discharging, the green lines represent a porosity of 97.4%, the red lines represent a porosity of 86.1%, and the blue lines represent a porosity of 64.6%.

Table II. Smoothed virtual foam properties.

d_{strut} (mm)	l_{cell} (mm)	ϵ (%)	A_{sp} (m^{-1})
0.1	10	97.4	150.6
0.05	5	97.4	375.1
0.02	2	97.4	743.4
0.01	1	97.4	1479.5
1.0	10	86.1	297.7
0.5	5	86.1	744.7
0.2	2	86.1	1479.4
0.1	1	86.1	2990.1
2	10	64.6	397.5
1	5	64.6	993.9
0.4	2	64.6	1969.6
0.2	1	64.6	3982.9

listed in Table II. The solid lines represent the volumetric capacity and are plotted on the primary y-axis. The values are also converted to the depth of discharge and plotted with dashed lines on the secondary y-axis. Different markers and line colors indicate the porosity of the associated foam structures. The most porous foam structure nearly reaches the completely discharged state with DoDs greater than around 0.9 for all cell sizes. The foam structure with 86.1% porosity approximately reaches the end of the discharge cycle for the foam cell sizes 1 cm and 2 cm but falls short of the more porous foam structure about 0.1 of DoD for greater cell size. The most dense foam with 64.6% porosity achieves an acceptable DoD higher than 0.9 for the smallest cell size and declines to DoDs of around 0.8 for the largest simulated foam cell size (10 mm). The drop in volumetric capacity—from most porous to densest foam—is bigger than the drop in DoD because the denser foams carry less electrolyte and therefore have a lower theoretical maximal capacity. For this reason, the usable volumetric capacity for the most porous foam structure is around 100 AhL^{-1} while it more than halves for the most dense foam structure still achieving a DoD of 0.6 for a cell size of 10 mm. The performance of the foam structure with 86.1% porosity lies in between. The theoretical capacity of a cathode

without a glassy carbon foam and solely filled with electrolyte is 117 AhL^{-1} . The same discharging process for a C-rate of 0.5 is laid out in Fig. 9. The simulated achievable DoDs are generally lower for all foam structures reaching values between 0.73 and 0.64 for the most porous foam structure. The most dense foam structure achieves poor DoDs between 0.4 and 0.2.

Figure 10 shows the electrolyte species concentrations averaged along the axis between separator and cathode current collector for a C/2 discharging process and a foam cell size of 10 mm. It should be pointed out that the iodine concentration is three orders of magnitude smaller than the other species concentrations and therefore refers to the secondary y-axis. It stands out that the iodine concentration in the vicinity of the cathode current collector decreases with the foam porosity— $1\text{e-}3 \text{ M}$ for the most porous foam compared to $5\text{e-}3 \text{ M}$. The foam structure with 97.4% porosity holds the least surface area, and the electric potential drop in the glassy carbon foam is the highest. This can be attributed to the fact that the struts of highly porous foams are thinner, thus needing higher electric potential gradients to drive the same electric current toward the opposite side of the cathode cell. In combination, most of the Butler-Volmer reaction takes place close to the cathode current collector consuming iodine. More important is the concentration of sodium ions in the proximity of the NaSICON separator. It locally exceeds 11.3 M which leads to the precipitation of sodium iodide. This is particularly harmful to the NaSICON and may lead to irreversible damage of the separator.

Generally, DoD declines with increasing cell size and with decreasing porosity. Smaller cell sizes are beneficiary because they are accompanied by higher specific surface areas of the glassy carbon foam serving the Butler-Volmer surface reaction. On the contrary, increasing the surface by decreasing the porosity has a negative effect on the achievable DoD. The pores of the denser foams are smaller albeit the cell size remains the same. These smaller pores hinder sodium ions coming from the anode from traveling through the cathode compartment toward the cathode current collector. Consequently, larger amounts of sodium ions remain in the space close to the separator exceeding the solubility limit of sodium iodide. As a result, the discharging process terminates. The performance of the dense foams becomes worse considering the porosity and comparing the capacity of the different structures (Figs. 9 and 8). The glassy carbon occupies more space for

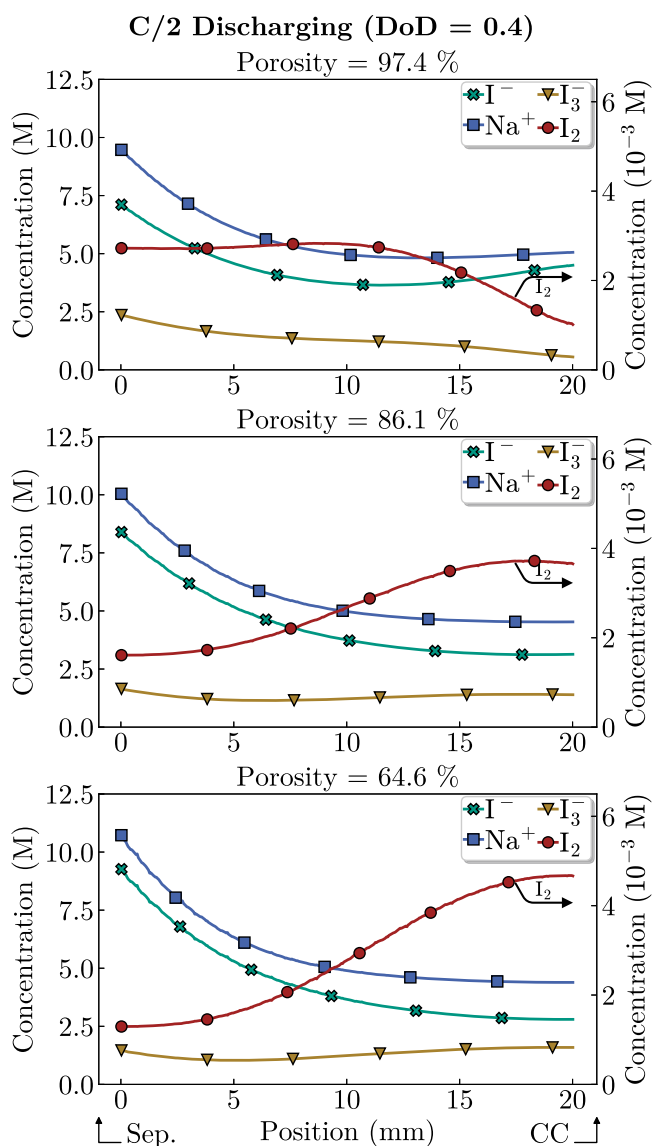


Figure 10. Simulated concentrations of electrolyte species during a C/2 initial discharge and for a 2 mm cell size. The catholyte species concentrations are averaged for positions between separator and cathode current collector (CC).

the dense foam than for the thinner foams and therefore lowers the theoretical capacity for the denser foams in the first place.

Charging.—Figure 11 shows the charging process for the aforementioned smoothed virtual foam structures. Charging takes place under galvanostatic conditions at a C-rate of 0.25. The graph indicates a similar trend compared to the C/4 discharging process. There is a slight but steady decrease of the achievable state of charge for all investigated foam structures. The SoC at the end of the charging cycle drops from 0.93 to 0.88 for the most porous foam. The charging process for the densest foam with a porosity of 64.6% terminates later than its discharging process, reaching and SoC = 0.86 for a foam cell size of 1 mm. The result of the C/4 charging simulation with the same foam structure and the largest cell size of 10 mm is nearly identical to its discharging process canceling at SoC = 0.62. The 86.1% porous foam performs better for a C/4 charging process compared to a C/4 discharging process for foam cell sizes smaller than 2 mm achieving SoCs higher than 0.9. Analogous to the densest foam structure, the achievable SoCs decline for the larger foam cell sizes. Again, the resulting volumetric

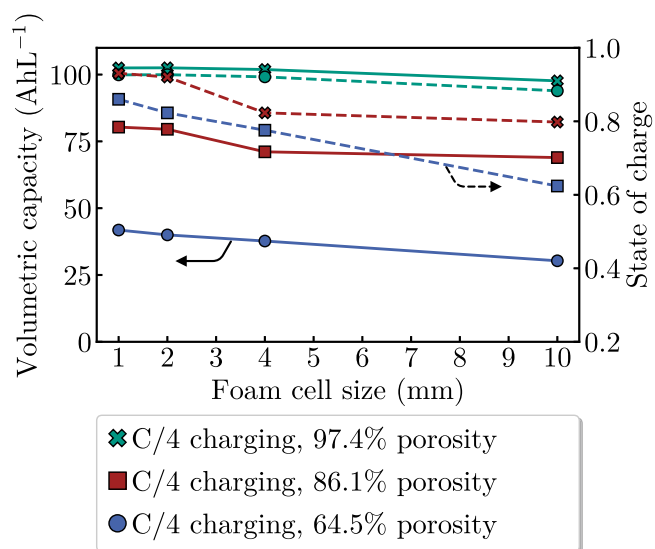


Figure 11. The Solid lines represent the utilizable volumetric capacity of a sodium iodine battery with glassy carbon foam structures as current collectors while the dashed lines represent the corresponding depth of discharge as a function of the foam cell size. Under C/4 charging, the green lines represent a porosity of 97.4%, the red lines represent a porosity of 86.1%, and the blue lines represent a porosity of 64.6%.

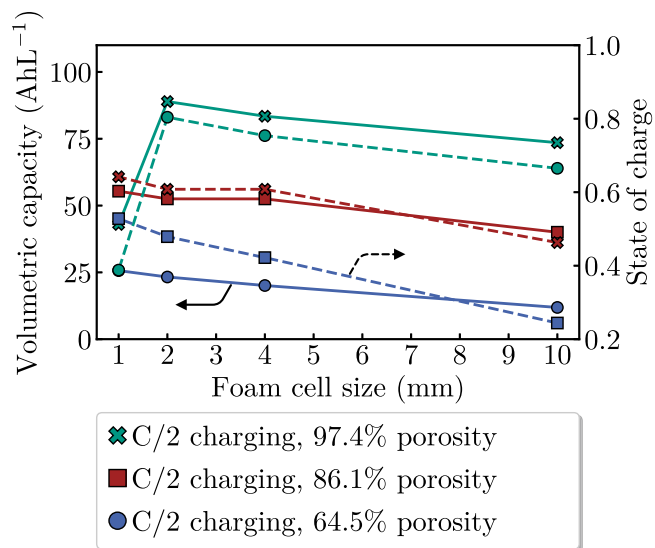


Figure 12. The solid lines represent the utilizable volumetric capacity of a sodium iodine battery with glassy carbon foam structures as current collectors while the dashed lines represent the corresponding depth of discharge as a function of the foam cell size. Under C/2 charging, the green lines represent a porosity of 97.4%, the red lines represent a porosity of 86.1%, and the blue lines represent a porosity of 64.6%.

capacities of the denser foam structures are distinctly lower than those of the most porous foam structures. The lower reachable SoCs in combination with less void volume penetrated with electrolyte lead to volumetric capacities of less than 50 AhL^{-1} for the smoothed foam structures with a 64.6% porosity. The cathode half cells utilizing foams of 97.4% porosity realize over 100 AhL^{-1} .

Figure 12 reports the same charging process with $C = 0.5$. There is a noticeable drop of achievable SoC for the most porous foam with 1 mm—which performed best earlier—to 0.39. The terminal SoC is significantly higher for the larger foam cell sizes and lies between 0.8 and 0.67. The densest foam (64.6% porosity) performance in the C/2 charging process follows the trend of the C/4

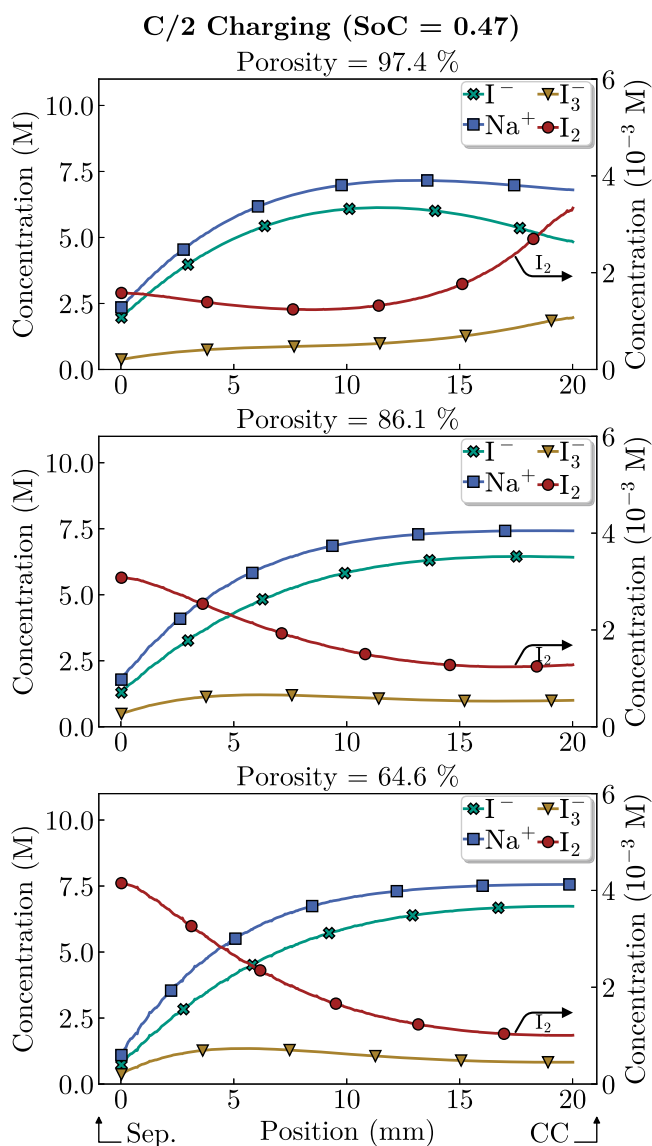


Figure 13. Simulated concentrations of electrolyte species during a C/2 initial charge and for a 2 mm cell size. The catholyte species concentrations are averaged for positions between separator and cathode current collector (CC).

charging process: The achievable SoC for a charging process with a cathode compartment constructed from small cell sizes is higher compared to discharging with identical C-rate. The batteries with larger cell sizes (>4 mm) act similarly for the charging process and the discharging process. The batteries consisting of a foam structure with 86.1% porosity achieve SoCs between 0.1 and 0.05 higher when charging compared to discharging with C/2 with a slightly steeper decline toward larger foam cell sizes. Figure 13 illustrates the electrolyte species concentrations averaged along the axis perpendicular to the separator and the cathode current collector. Iodine species concentrations are denoted on the secondary y-axis. The figure snapshots the concentration distribution at the same SoC for all porosities which is equivalent to the terminal SoC achievable (SoC = 0.47) for the densest foam structure (Fig. 12). The spatial distribution of mobile species reveals that the elemental iodine-to-sodium-ion relation locally sinks below $[I_{tot}]/[Na^+] < 0.475$ in the vicinity of the separator. This generates iodine precipitation and potentially dendrite forming which causes damage to the NaSICON ceramic that serves as the separator between the molten sodium and the aqueous electrolyte.

The three-dimensional simulations unveil that species transport from and to the electrode structure surface inside the particular foam cell is not the limiting factor. Hence, the observations show that sodium ion transport from and to the NaSICON separator throughout the cathode half cell is crucial for operating in safe working conditions without precipitation of NaI or I_2 .

Conclusions

Our study examines the effects of open-pored glassy carbon foams as three-dimensional electrode structures in sodium iodine battery cathodes. Spatially resolved simulations of the cathode compartment were carried out to give insights into the spatial distribution of electrolyte species inside the porous electrode structures. Comparative simulations between a two-dimensional cathode electrode design utilizing a vertically placed disc reveal that foam electrode structures drastically improve the achievable depth of discharge. Packing of Kelvin unit cells virtually reproduces the glassy carbon foam structure. The computational foam creation shows that maximizing the specific surface area inevitably causes the reduction of porosity. Our simulations suggest that a larger surface area at the expense of porosity is detrimental. The range of 150 m^{-1} to 3980 m^{-1} can improve the reachable depth of discharge by less than 0.1 on average based on our model assumptions. The volumetric capacity of the cathode half cell drops about 60 AhL^{-1} for a C/4 initial charging or discharging process when the porosity of the cathode electrode foam structure reduces from 97.4% to 64.5%. Simulations with higher C-rates of C/2 confirm that result leading to a 50 AhL^{-1} lower volumetric capacity for the most porous foam compared to the most dense foam.

Most significantly, large pores in relation to the foam cell size—which is associated with a high porosity—ensure a smooth sodium ion transit from one foam cell to another and immensely enhance battery performance. Lowering the cell size—which correlates to an increased surface area—has a modest positive effect except for 97.4% porous foams with cell sizes smaller than 2 mm.

In summary, the data proposes high porosity as the primary morphology property and specific surface area as the second characteristic in glassy carbon foam structures to maximize. Although further investigations are needed, the present study contributes to a better understanding of all-liquid sodium iodine batteries. With our new improvements in the cell design, the positive half-cell utilizes over 90% of the theoretical capacity reaching more than 100 AhL^{-1} . These insights aid in the further technical developments of iodine-based, all-liquid batteries. Together with a liquid sodium anode, the battery system is a future candidate for stationary energy storage considering its sustainable and earth-abundant materials and the scalability and safety of the battery system.

Acknowledgments

The authors acknowledge funding and support by the German Federal Ministry of Education and Research (Bundesministerium für Bildung und Forschung) under the project number 03XP0183C. The responsibility for the content is with the authors. The research was also supported by the state of Baden-Württemberg through bwHPC.

ORCID

F. Gerbig  <https://orcid.org/0000-0003-3059-0171>

References

1. C. B. Tabein, J. Dallas, S. Casanova, T. Pelech, G. Bournival, S. Saydam, and I. Canbulat, *Minerals Engineering*, **163**, 106743 (2021).
2. T. M. Gür, *Energy Environ. Sci.*, **11**, 2696 (2018).
3. M. Holzapfel, D. Wilde, C. Hupbauer, K. Ahlbrecht, and T. Berger, *Electrochimica Acta*, **237**, 12 (2017).
4. H. Zhu and R. J. Kee, *Electrochimica Acta*, **219**, 70 (2016).
5. F. Gerbig, S. Cernak, and H. Nirschl, *Energy Technology*, **9**, 2000857 (2021).
6. F. C. Walsh, L. F. Arenas, C. Ponce de León, G. W. Reade, I. Whyte, and B. G. Mellor, *Electrochimica Acta*, **215**, 566 (2016).

7. D. Pletcher and F. C. Walsh, "Three-dimensional electrodes." *Electrochemistry for a Cleaner Environment*, ed. J. D. Genders and N. L. Weinberg (East Amherst, NY, Electrosynthesis Company) p. 51 (1992).
8. K. C. Kelley and J. J. Votoupal, *BATTERY INCLUDING CARBON FOAM CURRENT COLLECTORS*, US6979513B2 (2005).
9. E. J. Fraser, J. P. Le Houx, L. F. Arenas, K. R. Dinesh, and R. Wills, *Journal of Energy Storage*, **52**, 104791 (2022).
10. S. Kim and C. W. Lee, *Procedia Materials Science*, **4**, 305 (2014).
11. N. Dukhan, *Proceedings of the XI International Conference on Porous Metals and Metallic Foams (MetFoam 2019)* (Cham, Springer International Publishing) (2020).
12. W. Thomson, *The London, Edinburgh, and Dublin Philosophical Magazine and Journal of Science*, **24**, 503 (1887).
13. D. Weaire and R. Phelan, *Philosophical Magazine Letters*, **69**, 107 (1994).
14. R. Shakibanezhad, M. Sadighi, and R. Hedayati, *Transport in Porous Media*, **142**, 229 (2022).
15. S. Cunsolo, M. Iasiello, M. Oliviero, N. Bianco, W. K. S. Chiu, and V. Naso, *Journal of Heat Transfer*, **138**, 022601 (2016).
16. M. Bai and J. N. Chung, *Int. J. Therm. Sci.*, **50**, 869 (2011).
17. A. Tentorio and U. Casolo-Ginelli, *J. Appl. Electrochem.*, **8**, 195 (1978).
18. A. Czerwiński, Z. Rogulski, S. Obregowski, H. Siwek, I. Paleska, M. Chotkowski, and M. Łukaszewski, *J. Appl. Electrochem.*, **39**, 559 (2009).
19. M. Mastragostino and C. Gramellini, *Electrochimica Acta*, **30**, 373 (1985).
20. H. G. Weller, G. Tabor, H. Jasak, and C. Fureby, *Comput. Phys.*, **12**, 620 (1998).
21. M. Kespe and H. Nirschl, *Int. J. Energy Res.*, **39**, 2062 (2015).
22. S. Cernak, F. Gerbig, M. Kespe, and H. Nirschl, *Energy Storage*, **2**, 5 (2020).
23. G. Milazzo and S. Caroli, *Tables of standard electrode potentials: Project of the IUPAC Electrochemistry Commission* (Chichester, Wiley)A Wiley-Interscience publication, 125 (1978).
24. J. R. Rumble, T. J. Bruno, and M. J. Doa, *CRC Handbook of Chemistry and Physics: A Ready-Reference Book of Chemical and Physical Data* (Boca Raton and London and New York, CRC Press Taylor & Francis Group) 101st ed. (2020).
25. N. Anantharamulu, K. Koteswara Rao, G. Rambabu, B. Vijaya Kumar, V. Radha, and M. Vithal, *J. Mater. Sci.*, **46**, 2821 (2011).
26. M. M. Gross, L. J. Small, A. S. Peretti, S. J. Percival, M. A. Rodriguez, and E. D. Spoerke, *J. Mater. Chem. A*, **8**, 17012 (2020).
27. L. J. Small, A. Eccleston, J. Lamb, A. C. Read, M. Robins, T. Meaders, D. Ingersoll, P. G. Clem, S. Bhavaraju, and E. D. Spoerke, *Journal of Power Sources*, **360**, 569 (2017).
28. H. S. Wroblowa and A. Saunders, *Journal of Electroanalytical Chemistry and Interfacial Electrochemistry*, **42**, 329 (1973).
29. J. Newman and N. P. Balsara, "Electrochemical systems." *The Electrochemical Society Series* (Hoboken, NJ, Wiley) 4th ed. (2021).
30. P. W. Atkins, J. de Paula, and J. Keeler, *Atkins' Physical Chemistry* (Oxford and New York, Oxford University Press) 11th ed. (2018).
31. M. Z. Bazant, *Acc. Chem. Res.*, **46**, 1144 (2013).
32. L. M. Dané, L. Janssen, and J. G. Hoogland, *Electrochimica Acta*, **13**, 507 (1968).
33. A. Hayashi, K. Noi, A. Sakuda, and M. Tatsumisago, *Nat. Commun.*, **3**, 856 (2012).
34. A. Anderko and M. M. Lencka, *Ind. Eng. Chem. Res.*, **36**, 1932 (1997).
35. L. Cantrel, J. M. Fulconis, and J. Chopin-Dumas, *Journal of Solution Chemistry*, **27**, 373 (1998).
36. H. Steinhaus, *Mathematical Snapshots* (Mineola, NY, Dover Publ) 3rd ed. (1999).
37. H. M. Cundy and A. P. Rollett, *Mathematical Models* (St. Albans, Tarquin Publications) 3rd ed. (2007).
38. J. Harris and H. Stöcker, *Handbook of Mathematics and Computational Science* (Springer, New York and Berlin and Heidelberg) (2006).
39. S. W. Goldstein, *Journal of the American Pharmaceutical Association. American Pharmaceutical Association*, **41**, 333 (1952).
40. S. Yamada and H. Sato, *Nature*, **193**, 261 (1962).
41. F. Gerbig, S. Cernak, and H. Nirschl, *ECS Trans.*, **104**, 123 (2021).
42. M. Doyle, T. F. Fuller, and J. Newman, *J. Electrochem. Soc.*, **140**, 1526 (1993).
43. C. A. Emereuwa, *Current Opinion in Electrochemistry*, **21**, 117 (2020).
44. Blender Development Team, (2021), Blender - a 3D modelling and rendering package.